Mechanical Systems and Signal Processing 112 (2018) 401–416

Contents lists available at ScienceDirect

Mechanical Systems and Signal Processing

journal homepage: www.elsevier.com/locate/ymssp

Reconstruction of unidirectional strain maps via iterative signal fusion for mesoscale structures monitored by a sensing skin

Mohammadkazem Sadoughi [a], Austin Downey [a,b], Jin Yan [b], Chao Hu [a,c,*], Simon Laflamme [b,c]

[a] Department of Mechanical Engineering, Iowa State University, Ames, IA, USA
[b] Department of Civil, Construction, and Environmental Engineering, Iowa State University, Ames, IA, USA
[c] Department of Electrical and Computer Engineering, Iowa State University, Ames, IA, USA

ARTICLE INFO

Article history:
Received 4 January 2018
Received in revised form 23 March 2018
Accepted 15 April 2018

Keywords:
Structural health monitoring
Sensing skin
Capacitive-based sensor
Soft elastomeric capacitor
Sensor network
Kriging-based signal decomposition

ABSTRACT

Flexible skin-like membranes have received considerable research interest for the cost-effective monitoring of mesoscale (large-scale) structures. The authors have recently proposed a large-area electronic consisting of a soft elastomeric capacitor (SEC) that transduces a structure's change in geometry (i.e. strain) into a measurable change in capacitance. The SEC sensor measures the summation of the orthogonal strains (i.e. $\varepsilon_x + \varepsilon_y$). It follows that an algorithm is required for the decomposition of the sensor signal into unidirectional strain maps. In this study, a new method enabling such decomposition, leveraging a dense sensor network of SECs and resistive strain gauges (RSGs), is proposed. This method, termed iterative signal fusion (ISF), combines the large-area sensing capability of SECs and the high-precision sensing capability of RSGs. The proposed ISF method adaptively fuses the different sources of signal information (e.g. from SECs and RSGs) to build a structure's best fit unidirectional strain maps. Each step of ISF contains an update process for strain maps based on the Kriging model. To demonstrate the accuracy of the proposed method, an experimental test bench is developed, which is the largest deployment of the SEC-based sensing skin to date in terms of both size and sensor count. A network of 40 SECs deployed on a grid (5×8) is utilized and an optimal sensor placement algorithm is used to select the optimal RSG sensor locations within the network of SECs. Results show that the proposed ISF method is capable of reconstructing unidirectional strain maps for the experimental test plate. In addition to the experimental data, a numerical validation for the ISF method is provided through a finite element analysis model of the experimental test bench.

1. Introduction

Traditionally, mesoscale structural systems, including aerospace structures, energy systems and civil infrastructures are investigated and maintained using break-down based and time-based [1] strategies. An alternative is condition-based maintenance, which is known to have strong economic benefits for owners, operators, and society [2,3]. Structural health monitoring (SHM) and life prediction are among the key components of condition based maintenance [4,5]. SHM is defined as the automation of damage detection, localization, and prognosis of structural systems and components. A major challenge in the

* Corresponding author at: Department of Mechanical Engineering, Iowa State University, Ames, IA, USA.
E-mail addresses: chaohu@iastate.edu, huchaostu@gmail.com (C. Hu).

https://doi.org/10.1016/j.ymssp.2018.04.023
0888-3270/

SHM of mesoscale structural systems is the distinction of global versus local faults [6–8].Also, since the monitored mesoscale structures can be geometrically complex [7], the selection of sensors and models capable of performing SHM can be challenging [6]. Of particular importance in the development of an SHM system is the consideration of sensor density. The use of dense sensor networks (DSNs) for SHM applications have attracted interest in recent years [8–12].

When compared to traditional sparse sensor networks, a DSN will provide for greater detection and localization of localized damage, including cracks [13,14], material delamination [15,16], corrosion [17], and loosening of bolts [18,19]. While a DSN has its advantages, it faces challenges in terms of high hardware requirements, complex installation, and high data management costs [19]. Recently, through the use of micro-fabrication techniques [9,20] and advances in the field of flexible electronics [21], skin-like sensing membranes have been proposed as a solution for simplifying the deployment and utilization of DSNs. These DSNs would fully integrate sensing, data acquisition, data transmission, and power management into a sensing skin. The term sensing skin is used because of their ability to mimic the capability of biological skin to detect and localize events (e.g. damage, contact, temperature changes) over a large area [22].

Sensing skins for SHM applications have attracted significant attention in the last few years and various sensing skins have been proposed and prototyped. These efforts have leveraged various technologies, including: resistive strain gauges (RSGs) [9,11]; piezoceramic transducers and receivers [23,24]; carbon nanotube thin film strain sensors [25,26]; electrically conductive paint [27]; graphitic porous sensor arrays on polyimide [20]; and photoactive nanocomposites [28]. The authors have previously proposed a fully integrated sensing skin [10] based on a novel large-area electronic termed the soft elastomeric capacitor (SEC) [29]. The SEC was designed to be inexpensive and benefits from an easily scalable manufacturing process. In contrast with traditional strain sensors (e.g. RSG, fiber optic, and vibrating wire) that measure unidirectional strain at discrete points, the SEC measures the additive strain over an area. The SEC and its additive strain signal have been used for fatigue crack detection [14] as well as damage detection and localization over large areas [30]. However, in cases where the unidirectional strain maps of a structure are desired, it is imperative that the sensor's additive signal be decomposed into its unidirectional components. Examples where a structure's unidirectional strain maps are needed include: the incorporation of strain data into existing strain based displacement [31] and damage detection [32] algorithms; model updating, including finite element analysis (FEA) and analytical surrogate models [33]; and material characterization [34,35].

In situations where the structure's unidirectional strain maps are needed, the main challenge is to decompose the SEC's additive strain map into its linear strain components along two orthogonal directions. To address this challenge, the authors have previously developed an algorithm that leverages a dense sensor network (DSN) of SECs to decompose the additive strain maps. The algorithm assumes a polynomial deflection shape and appropriate boundary conditions and uses a least squares estimator (LSE) to estimate unidirectional strain maps over the DSN's area [36]. However in certain cases, such as the complex loading conditions present in a wind turbine blade [10,37], accurate knowledge of the boundary conditions can be difficult or impossible to determine. To alleviate this challenge, RSGs were added to the DSN to allow for the real-time updating of boundary conditions at key locations, therefore, forming a hybrid DSN (HDSN) [38]. This extended LSE algorithm has been demonstrated for damage detection, both numerically [37] and experimentally [10]. While computationally efficient, the extended LSE algorithm lacks the ability to reproduce nonlinear or complex strain maps due to its selection of a polynomial deflection shape function. The capability to reproduce nonlinear or complex strain maps is important, because damage often manifests itself as nonlinearities in a unidirectional strain map (e.g., a thin crack in a plate) [10].

In this study, the authors propose a generic method, termed iterative signal fusion (ISF), that overcomes the difficulty of capturing high nonlinearities in strain responses and makes strain map reconstruction suitable for local damage detection. The method adaptively fuses the different sources of strain information from an HDSN containing both SECs and RSGs to build optimum and unique unidirectional strain maps. Each step of the ISF contains an update process for the strain maps based on a surrogate modeling technique. Various potential surrogate modeling techniques are based on radial basis functions [39], support vector machines [40], artificial neural networks [41], fuzzy modeling [42,43], and Kriging [44]. In the field of surrogate modeling, Kriging, or sometimes called Gaussian process regression, is a method of spatial interpolation for which the approximations are modeled by a Gaussian process derived by proper covariance [44,45]. The authors' previous studies showed that Kriging has strong benefits when it comes to processing data with a small number of sample points, a small number of input variables, and/or when the response shows a highly nonlinear behavior [46]. Due to these benefits, Kriging is selected in this study as the surrogate modeling technique. Since the RSG and SEC sensors are located at different locations on the surface of a structure, a simple Kriging model cannot directly be used to generate the unidirectional strain maps based on the available data. To address this issue, the proposed ISF method adaptively finds the best unbiased prediction of unidirectional strain data at the SEC sensor locations to virtually expand the set of strain data. Consequently, the unidirectional strain maps can be generated directly from this expanded data set using Kriging, or any other surrogate modeling technique.

In comparison with the previously developed extended LSE algorithm [38], the newly proposed ISF method is capable of more accurately modeling highly nonlinear strain maps due to its use of a Gaussian variogram in comparison to the polynomial shape function assumed by the extended LSE algorithm. The use of this Gaussian variogram also reduces the risk of overfitting that is common in high order polynomial shape functions. Preliminary comparisons between the proposed ISF method and the extended LSE algorithm have shown that ISF is able to achieve a more accurate approximation of unidirectional strain maps [47]. While the proposed ISF method is capable of producing more accurate uni-directional strain maps than the extended LSE algorithm, the extended LSE algorithm is more computationally efficient and may be better sui-

ted for certain embedded applications where computational power is limited (e.g., calculations performed on a sensing skin [10,48]).

As with any sensor network, the placement of sensors is a critical component of an SHM system [49]. The optimal sensor configuration is one that minimizes the likelihood of a type I (false positive) or type II (false negative) error [50]. Therefore, it is critical to implement an optimal sensor placement strategy for determining the locations of sensors within an HDSN. For the particular case under study, a network of 40 SECs deployed on a grid (5×8) is utilized on an experimental test bench and an optimal sensor placement algorithm is used to select the optimal RSG sensor locations within the network of SECs. This optimal sensor placement algorithm [51], previously developed by the authors for use within the extended LSE algorithm, leverages the intuitive idea that not all potential sensor locations hold the same level of information. The key contributions of this paper are twofold: (1) it introduces an effective strain decomposition algorithm for the previously proposed SEC-based sensing skin that does not require the assumption of a shape function; and (2) it validates the proposed SEC-based sensing skin and the newly proposed ISF method through experimental results obtained from the largest deployment of the SEC-based sensing skin, both in terms of size and sensor count.

2. Background

This section covers the background that is needed to implement the ISF method. This includes a review of the SEC sensors and its electromechanical model, a previously investigated genetic algorithm to determine the optimal placement of RSGs within a network of SECs, and the discussion of a generic Kriging model.

2.1. Soft elastomeric capacitor (SEC)

The SEC is a robust large-area electronic that is inexpensive and easy to fabricate. Its architecture, manufacturing process, and electromechanical models are presented in Refs. [29,52,53] and reviewed here for completeness. The SEC sensor takes the form of a parallel plate capacitor, as shown in Fig. 1, where the dielectric is composed of a styrene-ethylene-butadiene-styrene (SEBS) block co-polymer matrix filled with titania (TiO_2) to increase both its durability and permittivity. Its conductive plates are fabricated using a conductive paint, made from the same SEBS, but filled with carbon black particles, painted onto each side of the SEBS matrix. Copper contacts, with an electrically conductive adhesive, are added to the conductors on both the top and bottom plates. These contacts are used for connecting the data acquisition to the SECs with a secure solder connection. Lastly, a thin layer of conductive paint is applied over the copper contacts to ensure a good connection between the copper contacts and the conductors, as seen in Fig. 1. Manufacturing of the SEC sensor in various shapes and sizes is relatively simple and does not require any highly specialized equipment or techniques, therefore allowing the technology to be easily scaled. To ensure the SEC is capable of monitoring the substrate in both tension and compression, the sensor is pre-stretched during its adhesion to the monitored substrate.

The capacitance (C) of a parallel plate capacitor can be modeled as a non-lossy parallel plate capacitor assuming a sampling rate of less than 1 kHz:

$$C = e_0 e_r \frac{A}{h} \tag{1}$$

where $e_0 = 8.854$ pF/m is the vacuum permittivity, e_r is the polymer's relative permittivity, $A = d \cdot l$ is the sensor area of width d and length l, and h is the thickness of the dielectric as annotated in Fig. 1. Assuming small changes in strain, Eq. (1) leads to a differential equation that relates a change in strain to a change in capacitance (ΔC):

$$\frac{\Delta C}{C} = \frac{\Delta d}{d} + \frac{\Delta l}{l} - \frac{\Delta h}{h} \tag{2}$$

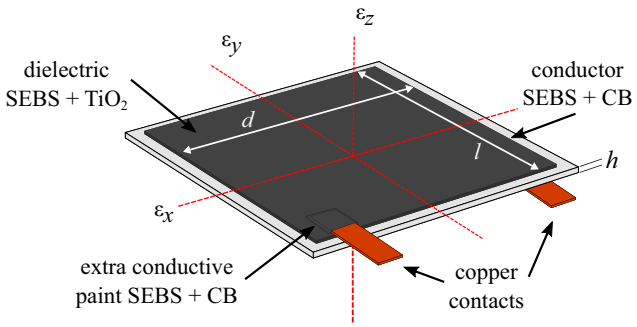

Fig. 1. A soft elastomeric capacitor (SEC) sensor with key components and reference axes annotated.

where $\Delta d/d$, $\Delta l/l$, and $\Delta h/h$, can be expressed as strain $\varepsilon_x, \varepsilon_y$, and ε_z, respectively. Assuming a plane stress condition, $\varepsilon_z = -\nu/(1-\nu)\cdot(\varepsilon_x+\varepsilon_y)$ where ν is the sensor material's Poisson's ratio taken as $\nu \approx 0.49$ [54]. The relative change in capacitance ΔC can be related to a change in the sensor's deformation as:

$$\frac{\Delta C}{C} = \lambda(\varepsilon_x + \varepsilon_y) \tag{3}$$

where $\lambda = 1/(1-\nu)$ represents the gauge factor of the sensor. Since $\nu \approx 0.49$, the gauge factor can be estimated as $\lambda \approx 2$. Eq. (3) shows that the signal of the SEC varies as a function of the sensor's additive strain, $\varepsilon_x + \varepsilon_y$.

The SEC's electro-mechanical model presented in Eq. (3) has been validated for both static and quasi-static loading conditions [55]. The linearity of the electro-mechanical model has been validated for mechanical excitation under 15 Hz [52]. Additionally, for mechanical responses up to 40 Hz, an altered electro-mechanical model accounting for the dynamic material properties of the SEC was presented in [53], but is not discussed here for brevity.

2.2. Optimal sensor placement

The sensing skin used in this work consists of a network of SECs with a few RSGs distributed into the SEC grid to form an HDSN. The numbers and locations of RSGs within an HDSN affect the accuracy of the decomposed strain fields. Therefore, it is important to consider an optimal sensor placement scheme for the RSGs when validating the ISF method. The authors have previously developed a genetic algorithm with a learning gene pool for selecting optimal RSG sensor locations within a network of SECs [51]. The genetic algorithm leverages the intuitive idea that for a set of potential sensor locations ($\mathbb{P}$), some sensor locations (p) add little or no information to the estimated system. Conversely, some sensor locations add a measurable level of information to the system. Therefore, the goal of the genetic algorithm is to build a set of optimal sensor locations ($\mathbf{P} = [p_1 \dots p_m]$) that minimize the error between the system and its estimated state. This goal is achieved through linking sensor locations to genes. The probability of these genes (sensor locations) reoccurring are then mutated over generations by the genetic algorithm. After a sufficient number of generations, only the strongest genes remain and these form a set of sensor locations that constitute an optimal set of RSG locations within the network of the SECs. In this work, the system is the true strain maps of the monitored substrate while the estimated state is the strain maps obtained through the ISF method. The error between the true strain field and its estimated state can be expressed in terms of type I and type II errors [50,51]. In the case where strain maps are obtained for a structure with the intention of detecting damage, a type I error (false positive) is the incorrect classification of a healthy state as a damage state, while, a type II error (false negative) is the failure to detect a structural fault.

Here, a previously developed single objective function [51], borrowed from the field of robust design [56], is used in the multi-objective problem for decreasing the likelihood of type I and type II errors through the optimal placement of RSGs in the HDSN. The occurrence of type I errors within the HDSN's extracted strain maps is reduced through minimizing the mean absolute error (MAE) between the system and its estimated state. The use of MAE for selecting sensor locations provides an effective representation of how a structure will perform under various loading conditions. However, if the placement of RSGs is based solely on the MAE of the system, locations of high disagreement between the estimated and real systems will develop. In the case of a load-carrying structural component, such an occurrence could result in the component being stressed passed its design limit (i.e. type II error). Therefore, to reduce the occurrence of type II errors, a second optimization problem based on minimizing the maximum difference between the system and its estimated state (i.e. strain value) at any point on a strain map is introduced, defined as E_{max}. The bi-objective optimization problem (type I and II errors) can be simplified into a single objective function through a straightforward scalarization approach formulated as a linear combination of the bi-objective optimization problem. Considering n possible sensor locations in $\mathbb{P}$, a single objective problem for optimizing the placement of m sensors ($0 \leqslant m \leqslant n$) can be formulated as,

$$\begin{aligned} &\underset{\mathbf{P}}{\text{minimize}} \quad \text{fit} = (1-\alpha)\frac{\text{MAE}(\mathbf{P})}{\text{MAE}'} + \alpha\frac{\text{E}_{max}(\mathbf{P})}{\text{E}'_{max}} \\ &\text{subject to} \quad \mathbf{P} = [p_1 \dots p_m]^{\text{T}} \in \mathbb{P} \end{aligned} \tag{4}$$

where α is a user-defined scalarization factor used to weigh both objective functions ($0 \leqslant \alpha \leqslant 1$) and MAE′ and E'_{max} are factors used for normalizing MAE and E_{max}. While the selection of α depends on the structure's ability to tolerate type I or type II errors, the value of 0.5 has been shown to be a suitable value for similar problems [51].

2.3. Kriging (Gaussian Process Regression)

Kriging performs two main steps simultaneously: (1) it builds a trend function $\mathbf{h}(\mathbf{x})\beta$ based on the available data; and (2) it constructs a Gaussian process using the residuals Z [44]. The Kriging-approximated model of the true response $G(\mathbf{x})$ takes the following form

$$\hat{G}(\mathbf{x}) = \mathbf{h}(\mathbf{x})\beta + Z(\mathbf{x}) \tag{5}$$

where $Z(\mathbf{x})$ is a Gaussian process with zero mean, variance s^2, and a correlation matrix Ψ. The objective is to capture the general trend or the largest variance in the data using the regression function and interpolate the residuals using the Gaussian process. The elements of matrix Ψ are derived by the kernel function that can take different forms to model the spatial correlation in random space. One popular choice is the squared exponential kernel with a vector of hyper-parameters θ [57]:

$$\psi(\mathbf{x}_i, \mathbf{x}_j) = \exp\left(-\frac{1}{2}(\mathbf{x}_i - \mathbf{x}_j)^T \mathrm{diag}(\theta)^{-2}(\mathbf{x}_i - \mathbf{x}_j)\right) \tag{6}$$

where $\mathbf{x}_i$ and $\mathbf{x}_j$ are two arbitrary points in the input space. The hyper-parameters determine the smoothness of the prediction, and are estimated by maximizing the likelihood of observations given Ψ. Subsequently, using the Sherman-Morrison-Woodbury formula, the prediction mean $\mu_{\hat{G}}$ and uncertainty $\sigma^2_{\hat{G}}$ of Kriging are expressed as [57]:

$$\mu_{\hat{G}}(\mathbf{x}) = \mathbf{h}(\mathbf{x})\beta + \mathbf{r}(\mathbf{x}) \cdot \Psi^{-1} \cdot (\mathbf{y} - \mathbf{F}\beta) \tag{7}$$

$$\sigma^2_{\hat{G}}(\mathbf{x}) = s^2\left[1 - \mathbf{r}(\mathbf{x})\Psi^{-1}\mathbf{r}(\mathbf{x})^{\mathrm{T}} + \frac{\left(1 - \mathbf{F}^{\mathrm{T}}\Psi^{-1}\mathbf{r}(\mathbf{x})^{\mathrm{T}}\right)}{\mathbf{F}^{\mathrm{T}}\Psi^{-1}\mathbf{F}}\right] \tag{8}$$

where $\mathbf{h}(\mathbf{x}) = [h_1, \ldots, h_p]^{\mathrm{T}}$ is a vector of p trend functions, $\mathbf{y} = [y_1, \ldots, y_t]^{\mathrm{T}}$ is a vector of t responses, β is the p-element vector of the coefficients of the trend functions, and $\mathbf{r}(\mathbf{x}) = [\psi(\mathbf{x}, \mathbf{x}_1), \ldots, \psi(\mathbf{x}, \mathbf{x}_t)]^{\mathrm{T}}$ is a vector of correlations between the testing point and t training points. The process variance s^2 can be determined as $s^2 = 1/t \cdot (\mathbf{y} - \mathbf{F}\beta)^{\mathrm{T}}\Psi^{-1}(\mathbf{y} - \mathbf{F}\beta)$. More details about the Kriging model can be found in reference [57].

3. Iterative Signal Fusion (ISF)

This work proposes the new ISF method for strain map reconstruction, with the objective to minimize the loss of information when fusing the various signals from HDSNs. To build strain maps from a DSN with a single type of sensor, one may simply use traditional surrogate modeling techniques (e.g. Kriging) when the source of strain data is limited to the one type of sensor, provided the strain data is obtained for the correct orientation. However, in the HDSN of interest both unidirectional and additive strain data are collected at different RSG and SEC sensor locations (see Fig. 4(b)). In addition, the different sensing systems are measuring the same physical phenomenon and thus a high correlation among the unidirectional and additive strain data can be expected. Therefore, a direct implementation of any traditional surrogate modeling technique would not leverage all potential information in the unidirectional strain map reconstruction. To overcome this challenge, the proposed ISF method adaptively fuses the multiple sources of strain information from both the SECs and RSGs to build an optimal prediction of the unidirectional strain maps. It follows that a high correlation among the reconstructed unidirectional and additive strain models is considered. In what follows, the traditional method and proposed methods are explained in the form of two scenarios.

3.1. Scenario 1 - Traditional method

First, consider the scenario where no information fusion is applied. The strain measurements collected by an HDSN can be grouped into three data sets (see the solid-line boxes in Fig. 2): (1) x-direction strains (ε_x) at the location of RSG−x sensors ($\mathbf{I}^{\mathrm{RSG-x}}$), (2) y-direction strains (ε_y) at the location of RSG−y sensors ($\mathbf{I}^{\mathrm{RSG-y}}$), and (3) additive strains ($\varepsilon_x + \varepsilon_y$) at the location of SEC sensors ($\mathbf{I}^{\mathrm{SEC}}$). Next, taking $\mathbf{O}$ as the measured strain data, superscripts are added to denote sensor type/locations and subscripts are added to denote strain map type. For example, $\mathbf{O}^{\mathrm{SEC}}_{\varepsilon_x+\varepsilon_y}$ represents the additive strain data at the locations of

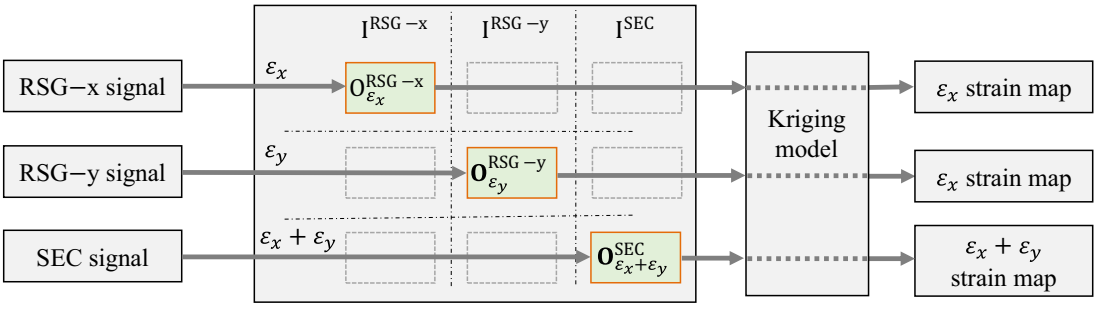

Fig. 2. Flowchart of unidirectional strain map reconstruction using a traditional Kriging method.

the SEC sensors while $\mathbf{O}^{\mathrm{RSG-x}}_{\varepsilon_x+\varepsilon_y}$ represents the additive strain data at the location of the RSG−x sensors. As shown in Fig. 2, traditional surrogate modeling techniques such as Kriging build the model for each of the three available strain data sets (i.e. $\mathbf{O}^{\mathrm{RSG-x}}_{\varepsilon_x}$, $\mathbf{O}^{\mathrm{RSG-y}}_{\varepsilon_y}$, and $\mathbf{O}^{\mathrm{SEC}}_{\varepsilon_x+\varepsilon_y}$) separately and independently. Therefore, the ε_x strain map, the ε_y strain map, and the $\varepsilon_x+\varepsilon_y$ strain map at an arbitrary point (x,y) on the surface of a structure are defined as:

$$\varepsilon_x = GP\Big((x,y)|\mathcal{D} = \{(\mathbf{I}^{\mathrm{RSG-x}}, \mathbf{O}^{\mathrm{RSG-x}}_{\varepsilon_x})\}\Big) \tag{9}$$

$$\varepsilon_y = GP\Big((x,y)|\mathcal{D} = \{(\mathbf{I}^{\mathrm{RSG-y}}, \mathbf{O}^{\mathrm{RSG-y}}_{\varepsilon_y})\}\Big) \tag{10}$$

$$\varepsilon_x+\varepsilon_y = GP\Big((x,y)|\mathcal{D} = \{(\mathbf{I}^{\mathrm{SEC}}, \mathbf{O}^{\mathrm{SEC}}_{\varepsilon_x+\varepsilon_y})\}\Big) \tag{11}$$

where $GP((x,y)|\mathcal{D})$ denotes the prediction at the arbitrary point (x,y) in the 2-D input space using the Gaussian process or Kriging model which is trained based on the data set $\mathcal{D}$. In Scenario 1, each model is built using a separate data set and it follows that this scenario does not consider any correlation among the built models. For instance, the SEC sensor data is not used for constructing either the ε_x strain map or the ε_y strain map.

3.2. Scenario 2 - Proposed method

Second, consider a scenario that leverages the correlation among the different sources of data in constructing the unidirectional strain maps. The ISF method is proposed based on this premise. To fuse the different sources of information, the proposed ISF method iteratively exploits all three strain measurement sets to estimate the strain responses at sensor locations where such responses are not measured. Fig. 3 shows the flowchart of the ISF method. A solid-line box denotes a directly measured strain and a dashed-line box denotes a strain that is not directly measured and needs to be estimated using the ISF method. To this end, Kriging is used to find the best unbiased prediction of strain data at the dashed-line boxes using the available data sets (i.e. RSG−x, RSG−y, and SEC senor data) as the training data sets. It follows that the unidirectional stain maps can be generated directly from Kriging or any other surrogate modeling techniques based on the expanded data sets at all solid-line and dashed-line boxes.

Algorithm 1. Procedure of ISF using Kriging to construct the strain maps

```
Build the initial Kriging model for all three strain maps        ▷Eqs. (12)–(14)
Calculate the error estimator ξ                                  ▷Eq. (21)
while ξ > ξ0 do
    Step 1: εy map at RSG−x sensors location                     ▷Eq. (15)
    Step 2: εx + εy strain map at RSG−x sensors location         ▷Eq. (16)
    Step 3: εx + εy strain map at RSG−y sensors location         ▷Eq. (17)
    Step 4: εx strain map at RSG−y sensors location              ▷Eq. (18)
    Step 5: εx strain map at SEC sensors location                ▷Eq. (19)
    Step 6: εy strain map at SEC sensors location                ▷Eq. (20)
    Calculate the error estimator ξ                              ▷Eq. (21)
end while
Build the final Kriging models                                   ▷Eqs. (22) and (23)
```

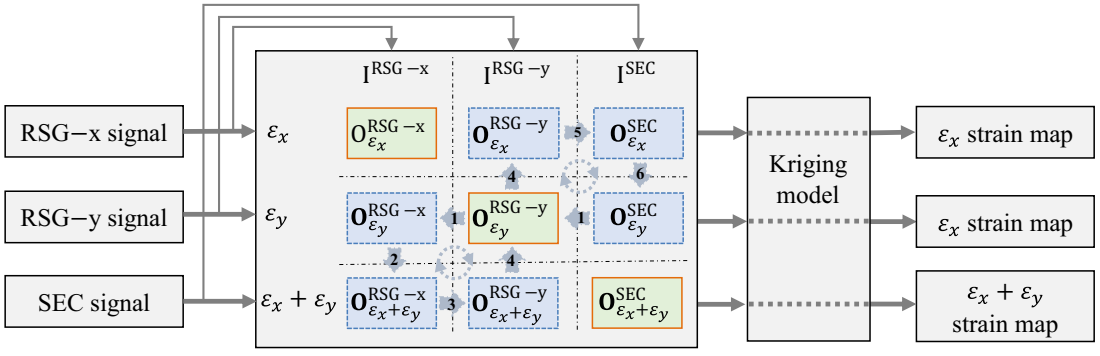

Fig. 3. Flowchart of the proposed ISF method.

In Fig. 3, all nine possible strain data sets are shown in the main middle block. The three solid-line boxes represent the available strain data sets and the six dashed-line boxes show the unavailable data sets for which one attempts to find the best unbiased predictions (called virtual data set). A pseudo-code of the proposed method is provided in Algorithm 1. The algorithm starts with finding initial guesses for the virtual data sets using the available data sets:

$$[\mathbf{O}_{\varepsilon_x}^{\mathrm{RSG-y}}, \mathbf{O}_{\varepsilon_x}^{\mathrm{SEC}}] = GP\left(\mathbf{I}^{\mathrm{RSG-y}}, \mathbf{I}^{\mathrm{SEC}} | \mathcal{D} = \{\mathbf{I}^{\mathrm{RSG-x}}, \mathbf{O}_{\varepsilon_x}^{\mathrm{RSG-x}}\}\right) \tag{12}$$

$$[\mathbf{O}_{\varepsilon_y}^{\mathrm{RSG-x}}, \mathbf{O}_{\varepsilon_y}^{\mathrm{SEC}}] = GP\left(\mathbf{I}^{\mathrm{RSG-x}}, \mathbf{I}^{\mathrm{SEC}} | \mathcal{D} = \{\mathbf{I}^{\mathrm{RSG-y}}, \mathbf{O}_{\varepsilon_y}^{\mathrm{RSG-y}}\}\right) \tag{13}$$

$$[\mathbf{O}_{\varepsilon_x+\varepsilon_y}^{\mathrm{RSG-x}}, \mathbf{O}_{\varepsilon_x+\varepsilon_y}^{\mathrm{RSG-y}}] = GP\left(\mathbf{I}^{\mathrm{RSG-x}}, \mathbf{I}^{\mathrm{RSG-y}} | \mathcal{D} = \{\mathbf{I}^{\mathrm{SEC}}, \mathbf{O}_{\varepsilon_x+\varepsilon_y}^{\mathrm{SEC}}\}\right) \tag{14}$$

After finding the initial guesses, the virtual data sets are updated iteratively until the optimal prediction is achieved. As shown by the small arrows in Fig. 3, each iteration consists of six sequential steps, each of which updates a Kriging (or strain response) model with the most recent strain measurements/estimates and uses the updated model to estimate the strain responses pertaining to one of the virtual data sets. Step 1 estimates ε_y at $\mathbf{I}^{\mathrm{RSG-x}}$ (virtual data set $\mathbf{O}_{\varepsilon_y}^{\mathrm{RSG-x}}$) based on all available y-strain measurements/estimates, $\mathbf{O}_{\varepsilon_y}^{\mathrm{RSG-y}}$ and $\mathbf{O}_{\varepsilon_y}^{\mathrm{SEC}}$, with the following form:

$$\mathbf{O}_{\varepsilon_y}^{\mathrm{RSG-x}} = GP\left(\mathbf{I}^{\mathrm{RSG-x}} | \mathcal{D} = \{(\mathbf{I}^{\mathrm{RSG-y}}, \mathbf{O}_{\varepsilon_y}^{\mathrm{RSG-y}}), (\mathbf{I}^{\mathrm{RSG-y}}, \mathbf{O}_{\varepsilon_y}^{\mathrm{SEC}})\}\right) \tag{15}$$

At Step 2, $\mathbf{O}_{\varepsilon_y}^{\mathrm{RSG-x}}$ (i.e. ε_y at $\mathbf{I}^{\mathrm{RSG-x}}$) is used to update the additive strain data $\mathbf{O}_{\varepsilon_x+\varepsilon_y}^{\mathrm{RSG-x}}$ at the same locations:

$$\mathbf{O}_{\varepsilon_x+\varepsilon_y}^{\mathrm{RSG-x}} = \mathbf{O}_{\varepsilon_y}^{\mathrm{RSG-x}} + \mathbf{O}_{\varepsilon_x}^{\mathrm{RSG-x}} \tag{16}$$

At Step 3, the virtual data set $\mathbf{O}_{\varepsilon_x+\varepsilon_y}^{\mathrm{RSG-y}}$ is updated using a Kriging model trained with the true data set $\mathbf{O}_{\varepsilon_x+\varepsilon_y}^{\mathrm{SEC}}$ and virtual data set $\mathbf{O}_{\varepsilon_x+\varepsilon_y}^{\mathrm{RSG-x}}$:

$$\mathbf{O}_{\varepsilon_x+\varepsilon_y}^{\mathrm{RSG-y}} = GP\left(\mathbf{I}^{\mathrm{RSG-y}} | \mathcal{D} = \{(\mathbf{I}^{\mathrm{SEC}}, \mathbf{O}_{\varepsilon_x+\varepsilon_y}^{\mathrm{SEC}}), (\mathbf{I}^{\mathrm{RSG-x}}, \mathbf{O}_{\varepsilon_x+\varepsilon_y}^{\mathrm{RSG-x}})\}\right) \tag{17}$$

At Step 4, the updated $\mathbf{O}_{\varepsilon_x+\varepsilon_y}^{\mathrm{RSG-y}}$ is used to predict $\mathbf{O}_{\varepsilon_x}^{\mathrm{RSG-y}}$:

$$\mathbf{O}_{\varepsilon_x}^{\mathrm{RSG-y}} = \mathbf{O}_{\varepsilon_x+\varepsilon_y}^{\mathrm{RSG-y}} - \mathbf{O}_{\varepsilon_y}^{\mathrm{RSG-y}} \tag{18}$$

At Step 5, $\mathbf{O}_{\varepsilon_x}^{\mathrm{SEC}}$ is updated using the following equation:

$$\mathbf{O}_{\varepsilon_x}^{\mathrm{SEC}} = GP\left(\mathbf{I}^{\mathrm{SEC}} | \mathcal{D} = \{(\mathbf{I}^{\mathrm{RSG-x}}, \mathbf{O}_{\varepsilon_x}^{\mathrm{RSG-x}}), (\mathbf{I}^{\mathrm{RSG-y}}, \mathbf{O}_{\varepsilon_x}^{\mathrm{RSG-y}})\}\right) \tag{19}$$

Lastly, Step 6 updates $\mathbf{O}_{\varepsilon_y}^{\mathrm{SEC}}$ using the values solved for in Steps 4 and 5 (Eqs. (18) and (19)):

$$\mathbf{O}_{\varepsilon_y}^{\mathrm{SEC}} = \mathbf{O}_{\varepsilon_x+\varepsilon_y}^{\mathrm{SEC}} - \mathbf{O}_{\varepsilon_x}^{\mathrm{SEC}} \tag{20}$$

After performing the 6 sequential steps, the strain estimates in all virtual data sets (dashed-line boxes) will be updated. The iteration continues until the level of change in the strain values pertaining to all dashed-line boxes converges close to zero. To this end, an error estimator is defined as:

$$\xi = \mathbf{O}_{\varepsilon_y}^{\mathrm{RSG-x}} - GP\left(\mathbf{I}^{\mathrm{RSG-x}} | \mathcal{D} = \{(\mathbf{I}^{\mathrm{RSG-y}}, \mathbf{O}_{\varepsilon_y}^{\mathrm{RSG-y}}), (\mathbf{I}_{\mathrm{SEC}}, \mathbf{O}_{\varepsilon_y}^{\mathrm{SEC}})\}\right) \tag{21}$$

If the change in $\mathbf{O}_{\varepsilon_y}^{\mathrm{RSG-x}}$ over sequential iterations converges to a same number (i.e. $\xi < \xi_0$), then the algorithm is stopped and the final Kriging models are built based on all measured/estimated ε_x and ε_y strain data to reconstruct the unidirectional strain maps, expanded for the entire surface area of the structure:

$$\varepsilon_x = GP\left((x,y) | \mathcal{D} = \{(\mathbf{I}^{\mathrm{RSG-x}}, \mathbf{O}_{\varepsilon_x}^{\mathrm{RSG-x}}), (\mathbf{I}^{\mathrm{RSG-y}}, \mathbf{O}_{\varepsilon_x}^{\mathrm{RSG-y}}), (\mathbf{I}^{\mathrm{SEC}}, \mathbf{O}_{\varepsilon_x}^{\mathrm{SEC}})\}\right) \tag{22}$$

$$\varepsilon_y = GP\left((x,y) | \mathcal{D} = \{(\mathbf{I}^{\mathrm{RSG-x}}, \mathbf{O}_{\varepsilon_y}^{\mathrm{RSG-x}}), (\mathbf{I}^{\mathrm{RSG-y}}, \mathbf{O}_{\varepsilon_y}^{\mathrm{RSG-y}}), (\mathbf{I}^{\mathrm{SEC}}, \mathbf{O}_{\varepsilon_y}^{\mathrm{SEC}})\}\right) \tag{23}$$

4. Methodology

This section presents the methodology used in validating the ISF method. First, an experimental test bench specifically designed for validating the ISF method is introduced, followed by the introduction of an FEA model of the test bench that is used for the numerical validation of the ISF method.

4.1. Experimental setup

The test bench developed for validating the ISF method is shown in Fig. 4. An HDSN consisting of 40 SECs and 20 RSGs (10 measuring ε_x and 10 measuring ε_y) was deployed onto the surface of a fiberglass plate with a geometry of 500 × 900 × 2.6 mm^3, as shown in Fig. 4(a). Fig. 4(b) is a schematic of the sensor layout showing the locations of the SECs and RSGs, where each RSG location has two RSGs (model #FCA-5-350-11-3LJBT, manufactured by Tokyo Sokki Kenkyujo), individually measuring ε_x and ε_y. The RSG locations are numbered 1–10, for later use in selecting RSGs to be utilized as part of the ISF method. Additionally, the four SECs denoted A, B, C, and D are used for investigating temporal strain data. A yellowing is present on some of the sensors' dielectrics (see sensors A and C for example). This yellowing does not appear to affect the sensors' strain measurements, as it will be discussed later in this work. The plate's left-hand side is bolted to an aluminum support (12.7 × 76.2 × 500 mm^3) to form a rigid connection. The rigid connection was added to eliminate the strain complexities that would be present if the hinges were connected directly to the fiberglass plate. This rigid connection is then attached to the frame through a pinned connection. The right-hand side of the plate is restrained in the vertical direction through the use of two lightly greased rods of diameter 12.7 mm to form a roller connection. Each SEC covers an area of 38 × 38 mm^2 and these SEC sensors are deployed in a 5 × 8 grid array. The center of an SEC sensor is used as the location of the sensor in the ISF method. The SEC and RSG data are sampled simultaneously at 17 samples per second. The SECs are measured using a custom-built data acquisition system that includes active shielding in the cable to remove the cable's parasitic capacitance. The RSGs are measured using three quarter bridge analog input modules (NI-9236, manufactured by National Instruments) mounted in a chassis (cDAQ-9178, manufactured by National Instruments). Additionally, the same chassis is used to obtain measurements from the LVDT (model #0244, manufactured by Trans-Tek) measured through a 16-bit analog input module (NI-9205) while also providing a simultaneous trigger source for the SEC and RSG DAQs through a sourced digital output (NI-9472, manufactured by National Instruments).

Two experimental load cases are considered during the course of this work. For load case 1, the plate is excited with a displacement controlled force at the center of the plate, as annotated in Fig. 4, sourced from a stepper motor located under the plate. The excitation force is a 20 mm sinusoidal load at 0.25 Hz. Load case 2 uses the same driving displacement and frequency, but includes a 0.5 kg mass added to the edge of the plate (see Fig. 4(b)) to introduce some complexities into the strain maps. To eliminate any high-frequency noise in the SEC signal, a fifth order Butterworth filter with a cutoff frequency of 10 Hz was applied to the raw SEC signals. No filtering was applied to the RSG signals.

4.2. FEA model

Numerical validation for the ISF method is performed through an FEA model of the experimental test bench created in Abaqus [58]. The FEA model included the fiberglass plate and the rigid aluminum connection that connects the pinned connections to the fiberglass plate. It was constructed using 298,065 eight-node brick elements with 1 integration point to allow for simple modeling of the connection between the fiberglass plate and the rigid aluminum connector. Constraints were modeled as a pinned connection at the plate's left-hand side and a roller connection on the plate's right-hand side. All materials were considered to be isotropic. In the fiberglass plate, nine elements are used through its thickness to prevent shear locking. A convergence test was performed and the selected model parameters yielded an error of less than 1% when compared to the FEA model with 1.2 million elements. The key parameters of the FEA model used in this numerical validation are listed in Table 1, where the material constants for the aluminum were taken from the material's data sheet and the material properties for the fiberglass were obtained experimentally from material drops. Similar to the experimental validation, two load cases are considered: (1) load case 1 consists of the plate displaced 20 mm upward at the middle and (2) load case 2

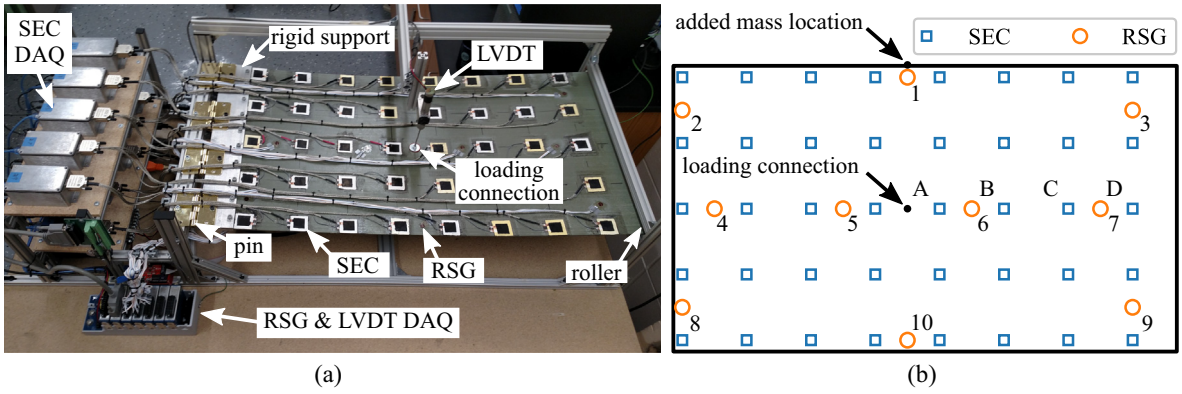

Fig. 4. Experimental setup used for validating the proposed method: (a) picture of the test bench with key components annotated and (b) schematic of the test bench showing the locations of the sensors, loading point, and added mass.

Table 1
Parameters used in constructing the FEA model.

Parameter	Value	Parameter	Value
Abaqus element type	C3D8R	Young's Modulus (aluminum)	68.9 GPa
Element type	Linear brick	Poisson's ratio 0.21 (aluminum)	0.33
Element nodes	8	Density (aluminum)	2700 kg/m^3
Element integration points	1	Young's Modulus (fiberglass)	15 GPa
Elements total	298,065	Poisson's ratio (fiberglass)	0.21
Elements (aluminum connection)	32,340	Density (fiberglass)	4500 kg/m^3
Elements (fiberglass plate)	265,725	Plate dimensions	$500 \times 900 \times 3.18$ mm^3

consists of the same displacement but with the addition of a 0.5 kg load at the center along the top edge, as shown in Fig. 4 (b).

Optimal sensor placement using the genetic algorithm presented in [51] and reviewed in Section 2.2 was performed using the results for both load case 1 and 2. The genetic algorithm was solved over 500 generations using a population of 50 offsprings per generation. An initial guess for the genetic algorithm was generated by finding the lowest MAE for a set of 50 randomly selected RSG sensor locations. Then, MAE$'$ and E'_{max} were set by solving for the MAE and point of maximum disagreement (E_{max}) for the initial guess. Table 2 reports the RSG sensors, numbered to correspond with the RSG sensor locations depicted in Fig. 4(b), used for developing the strain maps. When calculating the error between the FEA and ISF generated strain maps, every point on the FEA model was used excluding a 50×50 mm^2 square around the loading point. This was excluded as the FEA creates relatively high, highly localized strain values around the 30 mm circular loading point used in the FEA model to simulate the washer used in the real experimental setup.

5. Results

This section presents the numerical and experimental validation results for the proposed ISF method. First, the temporal data results for SEC sensors are provided to show the level of noise in strain measurements. Next, a structured numerical example that studies the effect of increasing the number of iterations of the proposed ISF method is presented. This is followed by an investigation on the effect of the number of RSGs on the accuracy of the built unidirectional strain maps. Then the proposed method is further verified via an experimental procedure.

5.1. Temporal strain data

Fig. 5 presents the temporal data results for sensors A, B, C, and D as denoted in Fig. 4(b). These sensors were selected to demonstrate the range of SEC sensor signals under varying strain conditions, including two sensors that experienced the yellowing of the dielectric discussed in Section 4.1. For clarity, only every other strain data point is reported for an individual SEC sensor with its corresponding marker type. The raw SEC signal is presented as a hollow marker while the signal filtered with a low-pass Butterworth filter is presented as a filled marker on a dotted line. As shown in Fig. 5, sensor D experiences the highest level of noise, which is due in part to the sensor having the longest cable at 1.2 m and the lowest level of strain. However, even with the high noise level and relatively low localized strain, the filtered signal provides a smooth signal that can be used for the ISF method.

5.2. Numerical investigation of strain maps

Figs. 6 and 7 demonstrate how increasing the number of iterations in ISF can increase the accuracy of the constructed strain maps for load cases 1 and 2, respectively. The errors reported in Figs. 6(a) and 7(a) are calculated based on the mean absolute difference between the true strain maps obtained through FEA and those obtained though ISF. For these examples, the ISF based strain maps were obtained using 8 optimally placed RSGs (Table 2). The first row in Figs. 6(b) and 7(b) show the unidirectional strain maps obtained using only the RSGs oriented in their respective orientations. This is the method discussed in Section 3.1 and annotated in Fig. 2. The error associated with these strain maps are labeled as the initial iteration in Figs. 6(a) and 7(a). The second to the fourth rows present the strain maps obtained by ISF from the initial guess, the first iteration and the second iteration, respectively. Four important observations can be made from the figures: (1) the strain maps constructed with the initial guess have very low accuracy; (2) by increasing the number of iterations, the strain maps obtained through ISF approach their real strain conditions; (3) in both load cases, the results by the proposed method converge to the optimal results only after a few iterations with no significant changes in the accuracy of strain maps thereafter; and (4) the algorithm converges to the optimal result that should be treated as a local minima of the true system, as MAE > 0. The last rows in Fig. 6(b) and 7(b) show the true strain maps obtained through FEA for both load cases.

Table 2
Locations of RSGs used in the ISF method.

Number of RSGs used	RSGs locations used for ε_x	RSGs used for ε_y
4	8, 10	3, 7
8	1, 4, 5, 7	1, 8, 9, 10
12	3, 5, 6, 7, 9	1, 4, 5, 6, 7, 8, 10

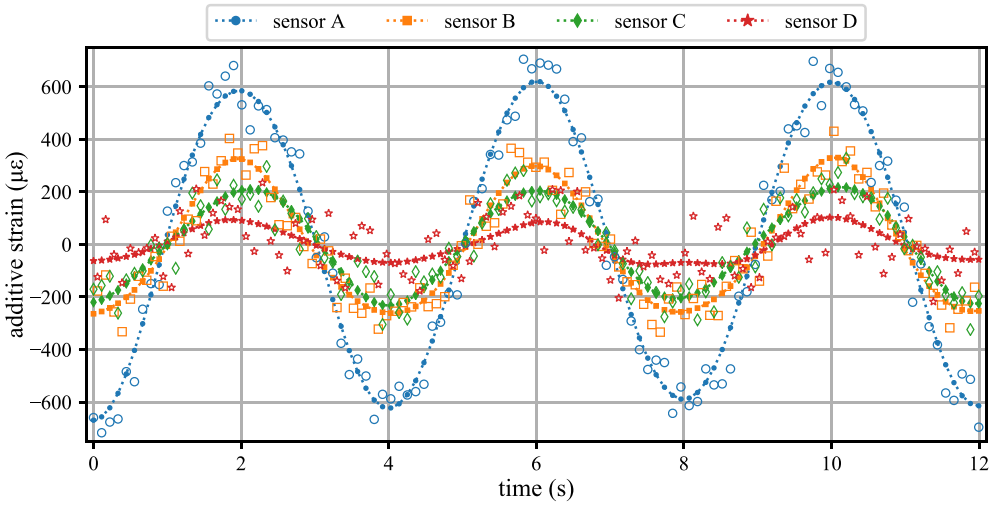

Fig. 5. SEC signal for sensors A, B, C, and D as denoted in Fig. 4 under load case 1; here, only every other data point is shown for clarity.

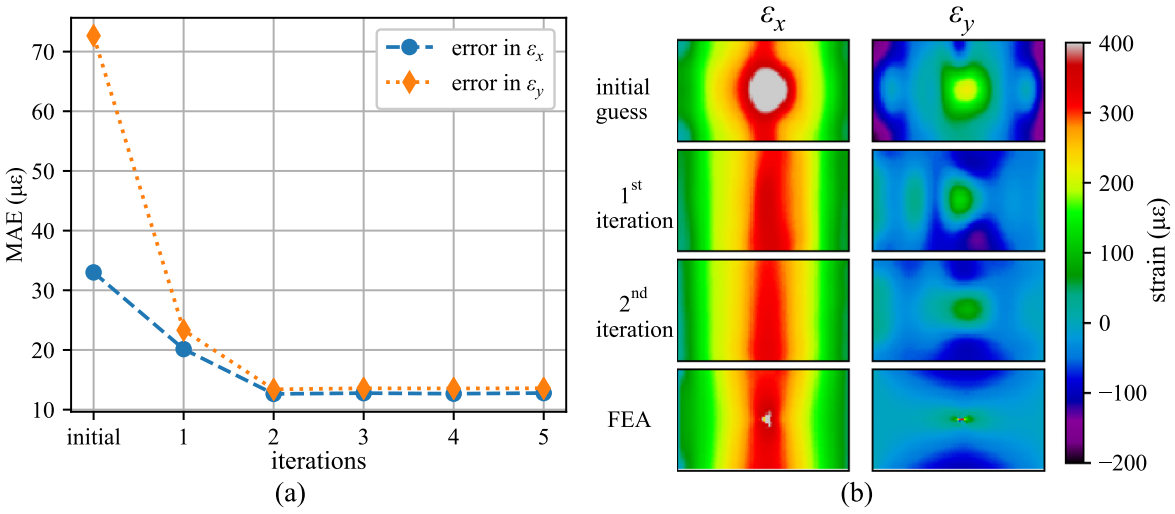

Fig. 6. Effect of number of iterations on the accuracy of the strain maps obtained through ISF for load case 1: (a) MAE versus the number of iterations and (b) strain maps obtained through ISF and FEA.

5.3. Effect of RSGs on strain maps

Fig. 8 reports the strain maps obtained through the FEA analysis (first row) for both load cases and the strain maps estimated using the ISF method with 4, 8, and 12 RSGs. From the FEA analysis, a difference can be observed in strain maps developed using load case 1 and those using load case 2, particularly in the ε_x strain maps. The mass exerts a compressive force on the top of the plate where the mass is added (see Fig. 4(b) for the location of the added mass). This compressive force reduces the magnitude of the tensile strain along the top of the plate. The unidirectional strain maps developed using the ISF method with 4, 8, and 12 optimally placed RSGs (Table 2) are presented on rows 2, 3, and 4, respectively.

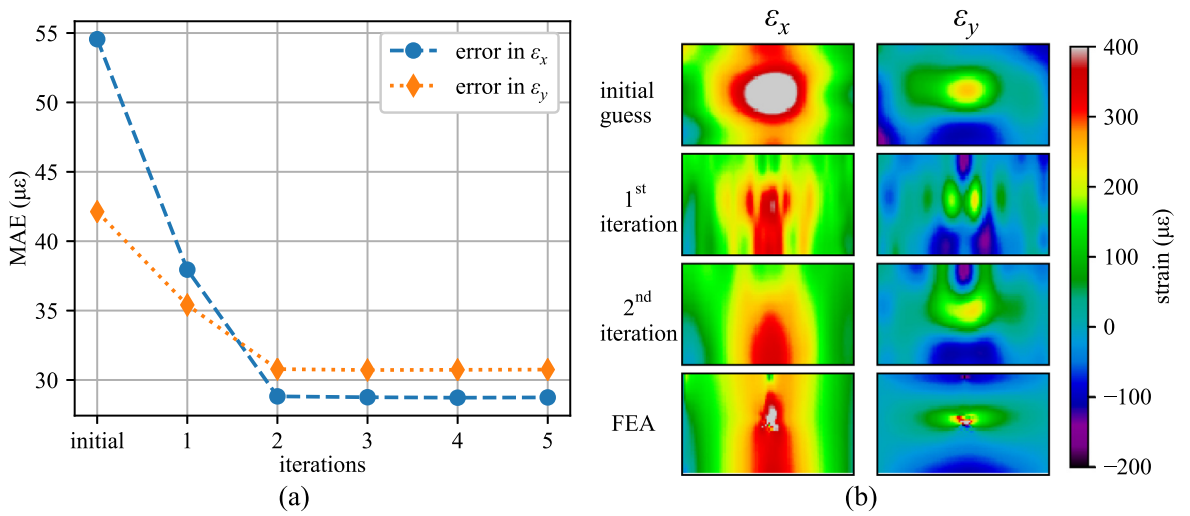

Fig. 7. Effect of number of iterations on the accuracy of the strain maps obtained through ISF for load case 2: (a) MAE versus the number of iterations and (b) strain maps obtained through ISF and FEA.

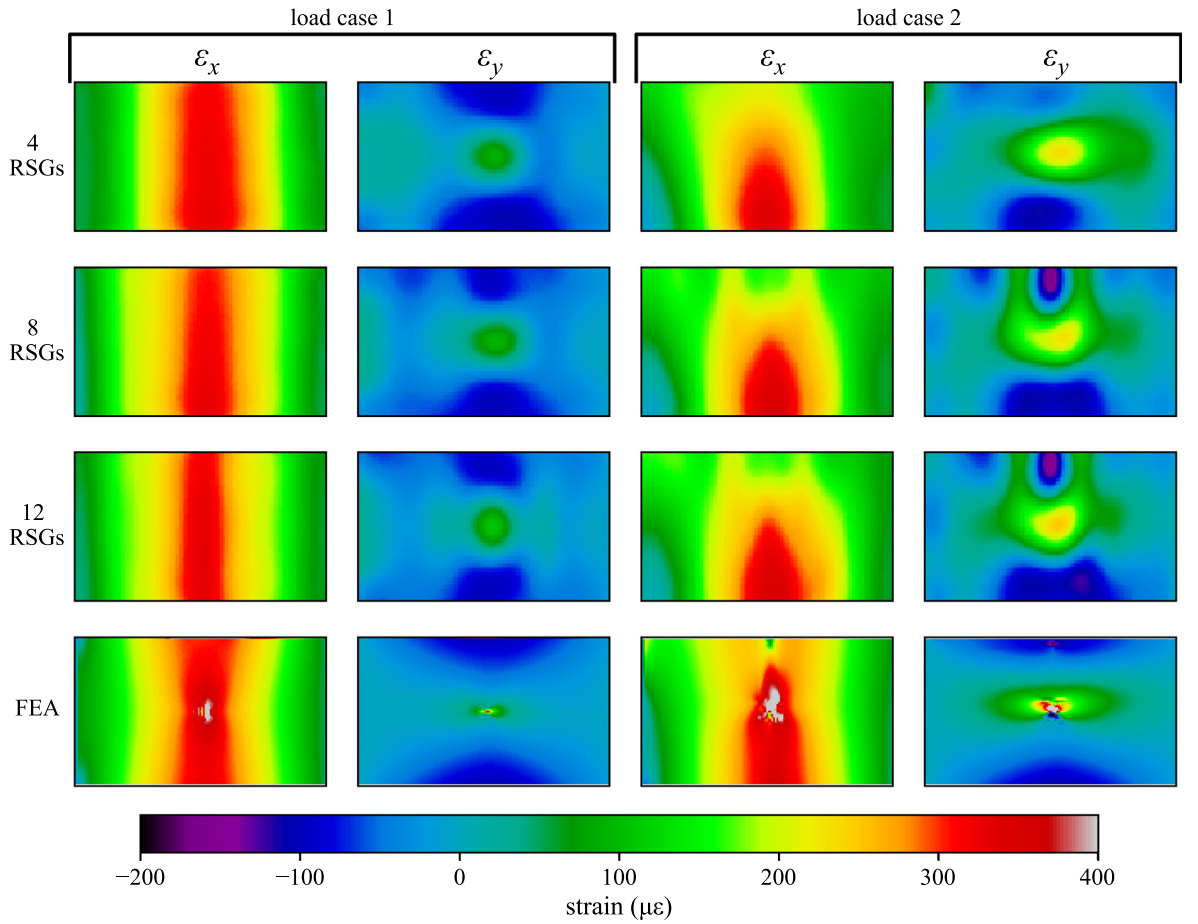

Fig. 8. Strain maps obtained through the FEA and the ISF method using the experimental data with 4, 8 and 12 RSGs.

Load case 1, a simpler loading configuration, is generally easily solved for using any numbers of RSGs. The largest points of disagreement between the FEA and ISF strain maps are around the loading connection. This is as hypothesized, because the sensor network is relatively sparse compared to the complexity of this local strain topology. In comparison, the more complicated strain topology caused by load case 2 benefits more from the increasing number of strain gauges. With a sufficient number of RSGs, the reconstructed strain maps try to fit the complex strain topologies around the location of the mass. In particular, the ISF method with 8 and 12 RSGs benefits from the higher numbers of RSGs as the optimal sensor placement algorithm selected RSG location #1 for the RSGs that measure ε_y. This added strain information at a location close to the added mass allows the ISF method to greatly increase its ability to track the complex strain topology, although this highly localized information causes the ISF method to overestimate the spatial distribution of the compressive load at top of the plate, as depicted by the large purple area in the ε_y strain maps for 8 and 12 RSGs in load case 2.

Next, the effect of increasing the number of RSGs used in the ISF method is investigated and presented in Fig. 9. This study uses the FEA model's derived strain maps to better investigate the effect of adding RSGs to the ISF method without considering the effect of other complications found in experimental testing (i.e., noise). Results are quantified using the error in the FEA strain maps (MAE and E_{max}) for both loading conditions. As before, a 50×50 mm^2 square around the loading point is

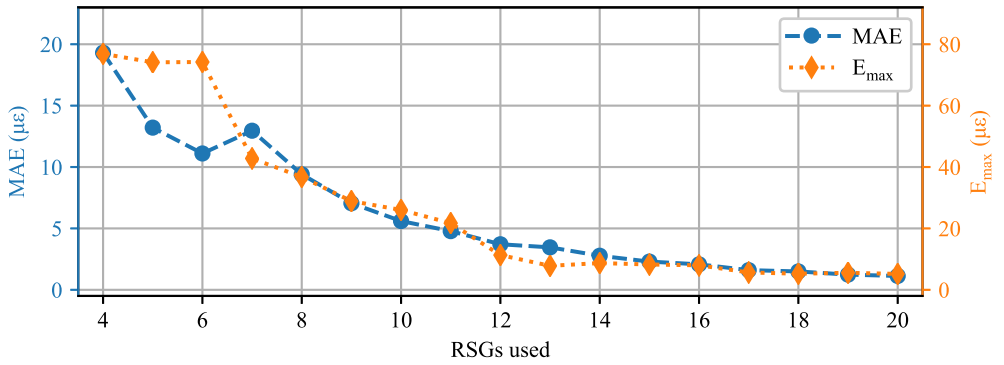

Fig. 9. ISF reconstruction error as a function of the number of RSGs used in the algorithm formulation. The error is calculated using both load cases 1 and 2.

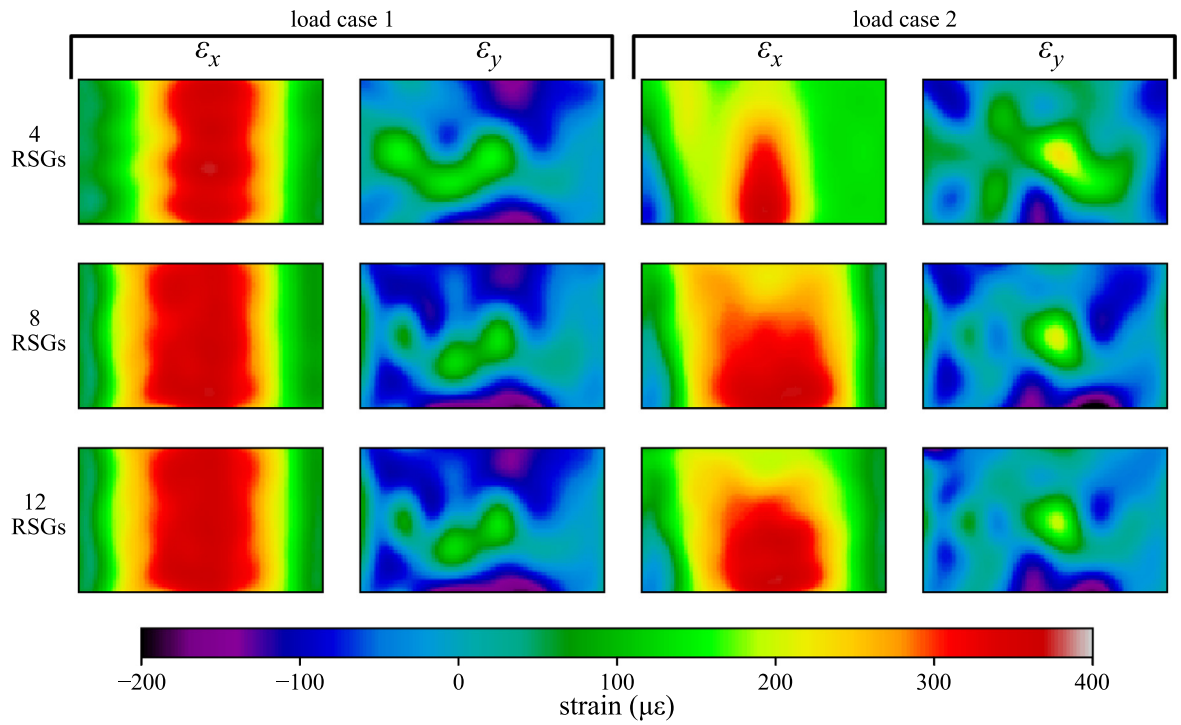

Fig. 10. Strain maps obtained through the ISF method using the experimental data with 4, 8, and 12 RSGs.

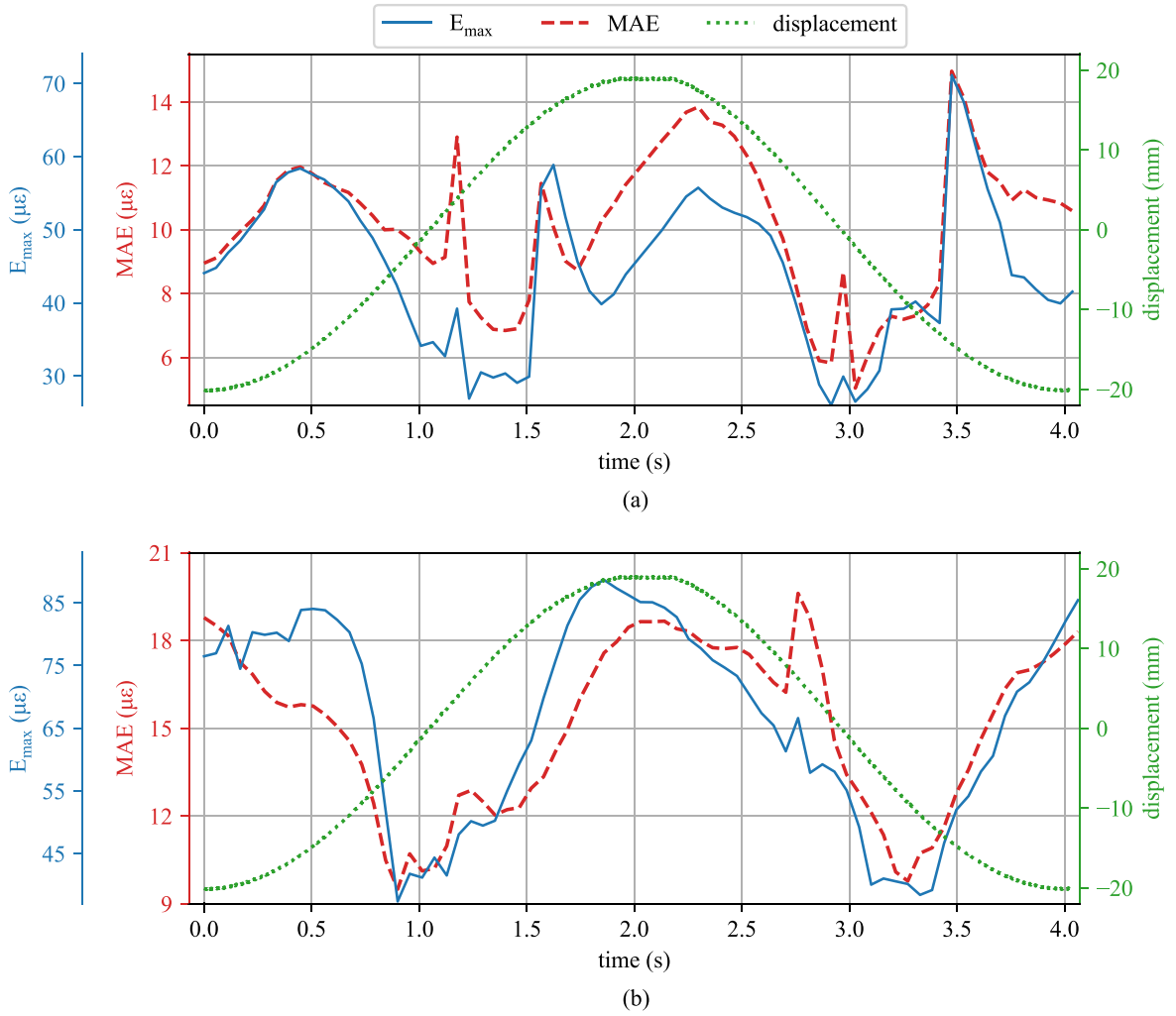

Fig. 11. Errors, MAE and β, as functions of the plate's displacement for: (a) load case 1 and (b) load case 2.

excluded when calculating the error to prevent the highly localized strain results from complicating the investigation. As expected and plotted in Fig. 9, the introduction of more RSGs into the ISF method results in a reduction of both quantifiable error values.

5.4. Experimental investigation of strain maps

Here, the experimental implementation of the ISF method is presented. Fig. 10 shows that the ISF method is capable of reconstructing strain maps for the experimental test plate. While no full-field strain data is available for the experimental test bench, the algorithm does generate strain maps close to those predicted by the FEA model. This is particularly true in load case 2 where the ISF method is capable of capturing the complex topology caused by adding the mass to the top of the plate. Deviations between the FEA model results and the experimental data could be caused by various factors, including material variations, imperfect loading conditions, and the fact that the FEA model does not account for the added mass and stiffness from the sensor wires.

Fig. 11 reports the temporal error results for the case with the ISF method with 12 RSGs over a typical load cycle. For this figure, the error is calculated by using the readings from all 20 RSGs. The RSGs were selected due to their high reliability and low level of noise. As expected, the error parameters increase when the magnitude of the displacement increases. This is due to the higher levels of strain in the system. Fig. 11(a) presents the temporal error data for load case 1 while Fig. 11(b) presents the temporal error data for load case 2. As expected, the errors are consistently higher for load case 2 (Fig. 11(b)) due to the more complex loading configuration. Fig. 12 presents a video of the test bench operating under load case 1 and the video file is included as a supplimentary material in the online version of this article.

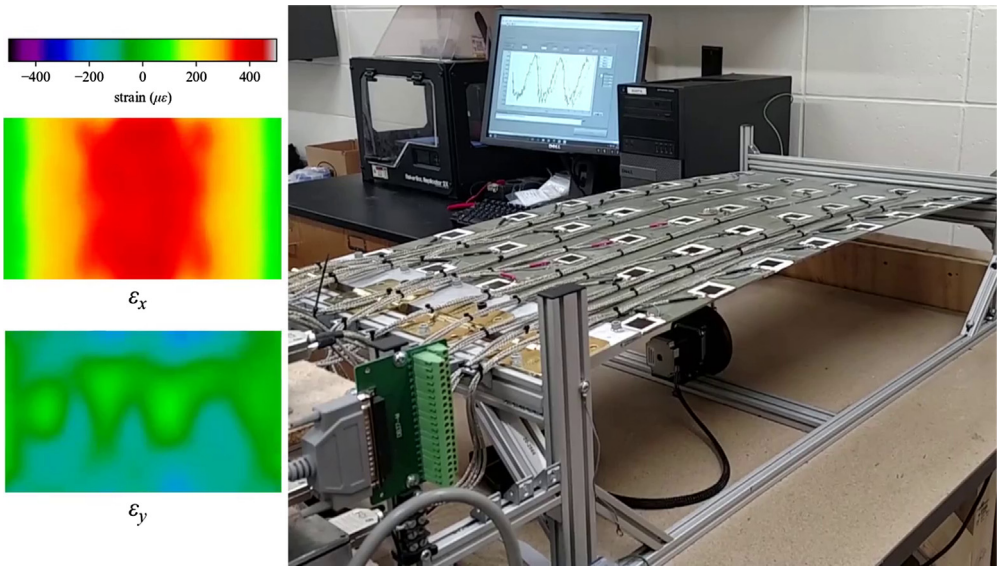

Fig. 12. Video of the experimental test bench operating under load case 1 with real-time strain data shown on the computer monitor and the post-processed uni-directional strain maps presented on the left-hand side.

6. Conclusion

We have proposed a robust method for the development of unidirectional strain maps from the additive strain signal of a novel large-area electronic, termed the soft elastomeric capacitor (SEC). When deployed in a network configuration, SECs can cover large-scale surfaces and can be used to reconstruct physics-based features for condition assessment, such as strain maps and deflection shapes. Given that each SEC measures the summation of the orthogonal strains (i.e. $\varepsilon_x + \varepsilon_y$), the proposed method retrieves the magnitude and directional information of strain prior to reconstructing strain maps. The proposed method, termed iterative signal fusion (ISF), adaptively fuses the different sources of signal information (e.g. from SECs and RSGs) to build best-fit unidirectional strain maps for the monitored structure. Each step of ISF contains an update process for strain maps based on a Kriging model. We have investigated the accuracy of the proposed method by developing an experimental test bench which is the largest deployment of the SEC-based sensing skin to date. We have utilized a network of 40 SECs deployed on a grid (5×8) and an optimal sensor placement algorithm to select the optimal RSG sensor locations within the network of SECs. This optimal sensor placement algorithm, previously developed by the authors, leverages the intuitive idea that not all potential sensor locations hold the same level of information. Two experimental load cases were considered during the course of this work. These load cases consist of a displacement controlled force at the center of the experimental plate and a similar load case but with a mass added to the edge of the plate to introduce some complexities into the strain maps. For both load cases, the results show that the proposed ISF method successfully develops strain maps for the experimental test plate. In addition, a finite element analysis model of the experimental test bench was developed to numerically verify the accuracy of the proposed ISF method. While no full-field strain data is available for the experimental test bench, we have shown that the results of unidirectional strain maps reconstructed using the ISF method strongly correlate with the results generated by the numerical finite element analysis model.

Acknowledgements

This work was in part supported by the U.S. National Science Foundation Grant Nos. CNS-1566579 and ECCS-1611333. This work was also partly supported by the U.S. National Science Foundation Grant No. 1069283, which supports the activities of the Integrative Graduate Education and Research Traineeship (IGERT) in Wind Energy Science, Engineering and Policy (WESEP) at Iowa State University. Their support is gratefully acknowledged. Any opinions, findings, and conclusions or recommendations expressed in this material are those of the authors and do not necessarily reflect the views of the National Science Foundation.

Appendix A. Supplementary material

Supplementary data associated with this article can be found, in the online version, at https://doi.org/10.1016/j.ymssp.2018.04.023.

References

[1] P.C. Chang, A. Flatau, S.C. Liu, Review paper: health monitoring of civil infrastructure, Struct. Health Monitor.: Int. J. 2 (3) (2003) 257–267, https://doi.org/10.1177/1475921703036169.
[2] C.C. Ciang, J.-R. Lee, H.-J. Bang, Structural health monitoring for a wind turbine system: a review of damage detection methods, Measur. Sci. Technol. 19 (12) (2008) 122001, https://doi.org/10.1088/0957-0233/19/12/122001.
[3] D. Adams, J. White, M. Rumsey, C. Farrar, Structural health monitoring of wind turbines: method and application to a HAWT, Wind Energy 14 (4) (2011) 603–623, https://doi.org/10.1002/we.437.
[4] C. Hu, B.D. Youn, T. Kim, P. Wang, A co-training-based approach for prediction of remaining useful life utilizing both failure and suspension data, Mech. Syst. Sig. Process. 62–63 (2015) 75–90, https://doi.org/10.1016/j.ymssp.2015.03.004.
[5] P. Wang, B.D. Youn, C. Hu, A generic probabilistic framework for structural health prognostics and uncertainty management, Mech. Syst. Sig. Process. 28 (2012) 622–637, https://doi.org/10.1016/j.ymssp.2011.10.019.
[6] J.M.W. Brownjohn, A.D. Stefano, Y.-L. Xu, H. Wenzel, A.E. Aktan, Vibration-based monitoring of civil infrastructure: challenges and successes, J. Civil Struct. Health Monitor. 1 (3-4) (2011) 79–95, https://doi.org/10.1007/s13349-011-0009-5.
[7] H. Park, Y. Shin, S. Choi, Y. Kim, An integrative structural health monitoring system for the local/global responses of a large-scale irregular building under construction, Sensors 13 (7) (2013) 9085–9103, https://doi.org/10.3390/s130709085.
[8] J. Kullaa, Distinguishing between sensor fault, structural damage, and environmental or operational effects in structural health monitoring, Mech. Syst. Sig. Process. 25 (8) (2011) 2976–2989, https://doi.org/10.1016/j.ymssp.2011.05.017.
[9] Y. Hu, L. Huang, W.S.A. Rieutort-Louis, J. Sanz-Robinson, J.C. Sturm, S. Wagner, N. Verma, A self-powered system for large-scale strain sensing by combining CMOS ICs with large-area electronics, IEEE J. Solid-State Circ. 49 (4) (2014) 838–850, https://doi.org/10.1109/jssc.2013.2294326.
[10] A. Downey, S. Laflamme, F. Ubertini, Experimental wind tunnel study of a smart sensing skin for condition evaluation of a wind turbine blade, Smart Mater. Struct., doi:https://doi.org/10.1088/1361-665X/aa9349.
[11] Y. Yao, B. Glisic, Detection of steel fatigue cracks with strain sensing sheets based on large area electronics, Sensors 15 (4) (2015) 8088–8108, https://doi.org/10.3390/s150408088.
[12] A. Deraemaeker, A. Preumont, Vibration based damage detection using large array sensors and spatial filters, Mech. Syst. Sig. Process. 20 (7) (2006) 1615–1630, https://doi.org/10.1016/j.ymssp.2005.02.010.
[13] Y. Yao, S.-T.E. Tung, B. Glisic, Crack detection and characterization techniques-an overview, Struct. Control Health Monitor. 21 (12) (2014) 1387–1413, https://doi.org/10.1002/stc.1655.
[14] X. Kong, J. Li, W. Collins, C. Bennett, S. Laflamme, H. Jo, A large-area strain sensing technology for monitoring fatigue cracks in steel bridges, Smart Mater. Struct. 26 (8) (2017) 085024, https://doi.org/10.1088/1361-665x/aa75ef.
[15] K.E. Cramer, Research Developments in Nondestructive Evaluation and Structural Health Monitoring for the Sustainment of Composite Aerospace Structures at NASA <https://ntrs.nasa.gov/archive/nasa/casi.ntrs.nasa.gov/20160012012.pdf>.
[16] S. Pavlopoulou, S. Grammatikos, E. Kordatos, K. Worden, A. Paipetis, T. Matikas, C. Soutis, Continuous debonding monitoring of a patch repaired helicopter stabilizer: damage assessment and analysis, Compos. Struct. 127 (2015) 231–244, https://doi.org/10.1016/j.compstruct.2015.03.014.
[17] X. Zhao, H. Gao, G. Zhang, B. Ayhan, F. Yan, C. Kwan, J.L. Rose, Active health monitoring of an aircraft wing with embedded piezoelectric sensor/actuator network: I. Defect detection, localization and growth monitoring, Smart Mater. Struct. 16 (4) (2007) 1208–1217, https://doi.org/10.1088/0964-1726/16/4/032.
[18] V. Caccese, R. Mewer, S.S. Vel, Detection of bolt load loss in hybrid composite/metal bolted connections, Eng. Struct. 26 (7) (2004) 895–906, https://doi.org/10.1016/j.engstruct.2004.02.008.
[19] R.M. Ghazi, J.G. Chen, O. Büyüköztürk, Pairwise graphical models for structural health monitoring with dense sensor arrays, Mech. Syst. Sig. Process. 93 (2017) 578–592, https://doi.org/10.1016/j.ymssp.2017.02.026.
[20] S. Luo, P.T. Hoang, T. Liu, Direct laser writing for creating porous graphitic structures and their use for flexible and highly sensitive sensor and sensor arrays, Carbon 96 (2016) 522–531, https://doi.org/10.1016/j.carbon.2015.09.076.
[21] J.A. Rogers, T. Someya, Y. Huang, Materials and mechanics for stretchable electronics, Science 327 (5973) (2010) 1603–1607, https://doi.org/10.1126/science.1182383.
[22] M.L. Hammock, A. Chortos, B.C.-K. Tee, J.B.-H. Tok, Z. Bao, 25th anniversary article: the evolution of electronic skin (e-skin): a brief history, design considerations, and recent progress, Adv. Mater. 25 (42) (2013) 5997–6038, https://doi.org/10.1002/adma.201302240.
[23] M.J. Schulz, M.J. Sundaresan, Smart Sensor System for Structural Condition Monitoring of Wind Turbines: May 30, 2002–April 30, 2006, National Renewable Energy Laboratory, 2006 <https://pdfs.semanticscholar.org/a38f/83bec8c8d0d5084554f679d2726f07c30baf.pdf>.
[24] V. Giurgiutiu, A. Zagrai, J. Bao, Damage identification in aging aircraft structures with piezoelectric wafer active sensors, J. Intell. Mater. Syst. Struct. 15 (9–10) (2004) 673–687, https://doi.org/10.1177/1045389x04038051.
[25] K.J. Loh, T.-C. Hou, J.P. Lynch, N.A. Kotov, Carbon nanotube sensing skins for spatial strain and impact damage identification, J. Nondestruct. Eval. 28 (1) (2009) 9–25, https://doi.org/10.1007/s10921-009-0043-y.
[26] A. Burton, J. Lynch, M. Kurata, K. Law, Fully integrated carbon nanotube composite thin film strain sensors on flexible substrates for structural health monitoring, Smart Mater. Struct. 26(9), doi:https://doi.org/10.1088/1361-665X/aa8105.
[27] M. Hallaji, A. Seppänen, M. Pour-Ghaz, Electrical impedance tomography-based sensing skin for quantitative imaging of damage in concrete, Smart Mater. Struct. 23 (8) (2014) 085001, https://doi.org/10.1088/0964-1726/23/8/085001.
[28] D. Ryu, K.J. Loh, Strain sensing using photocurrent generated by photoactive p3ht-based nanocomposites, Smart Mater. Struct. 21 (6) (2012) 065016, https://doi.org/10.1088/0964-1726/21/6/065016.
[29] S. Laflamme, M. Kollosche, J.J. Connor, G. Kofod, Robust flexible capacitive surface sensor for structural health monitoring applications, J. Eng. Mech. 139 (7) (2013) 879–885, https://doi.org/10.1061/(asce)em.1943-7889.0000530.
[30] S. Laflamme, L. Cao, E. Chatzi, F. Ubertini, Damage detection and localization from dense network of strain sensors, Shock Vib. 2016 (2016) 1–13, https://doi.org/10.1155/2016/2562949.
[31] B. Pan, K. Qian, H. Xie, A. Asundi, Two-dimensional digital image correlation for in-plane displacement and strain measurement: a review, Measur. Sci. Technol. 20 (6) (2009) 062001, https://doi.org/10.1088/0957-0233/20/6/062001.
[32] J. Cuadra, P.A. Vanniamparambil, K. Hazeli, I. Bartoli, A. Kontsos, Damage quantification in polymer composites using a hybrid NDT approach, Compos. Sci. Technol. 83 (2013) 11–21, https://doi.org/10.1016/j.compscitech.2013.04.013.
[33] E. Tuegel, The airframe digital twin: some challenges to realization, in: 53rd AIAA/ASME/ASCE/AHS/ASC Structures, Structural Dynamics and Materials Conference
20th AIAA/ASME/AHS Adaptive Structures Conference
14th AIAA, American Institute of Aeronautics and Astronautics, 2012, doi:https://doi.org/10.2514/6.2012-1812.
[34] S.V. Lomov, D.S. Ivanov, I. Verpoest, M. Zako, T. Kurashiki, H. Nakai, J. Molimard, A. Vautrin, Full-field strain measurements for validation of meso-FE analysis of textile composites, Compos. Part A: Appl. Sci. Manuf. 39 (8) (2008) 1218–1231, https://doi.org/10.1016/j.compositesa.2007.09.011.
[35] H.F. Poulsen, J.A. Wert, J. Neuefeind, V. Honkimäki, M. Daymond, Measuring strain distributions in amorphous materials, Nat. Mater. 4 (1) (2004) 33–36, https://doi.org/10.1038/nmat1266.
[36] J. Wu, C. Song, H.S. Saleem, A. Downey, S. Laflamme, Network of flexible capacitive strain gauges for the reconstruction of surface strain, Measur. Sci. Technol. 26 (5) (2015) 055103, https://doi.org/10.1088/0957-0233/26/5/055103.
[37] A. Downey, F. Ubertini, S. Laflamme, Algorithm for damage detection in wind turbine blades using a hybrid dense sensor network with feature level data fusion, J. Wind Eng. Indust. Aerodyn. 168 (2017) 288–296, https://doi.org/10.1016/j.jweia.2017.06.016.

[38] A. Downey, S. Laflamme, F. Ubertini, Reconstruction of in-plane strain maps using hybrid dense sensor network composed of sensing skin, Measur. Sci. Technol. 27 (12) (2016) 124016, https://doi.org/10.1088/0957-0233/27/12/124016. http://stacks.iop.org/0957-0233/27/i=12/a=124016.
[39] J. Park, I.W. Sandberg, Universal approximation using radial-basis-function networks, Neural Comput. 3 (2) (1991) 246–257, https://doi.org/10.1162/neco.1991.3.2.246.
[40] C. Cortes, V. Vapnik, Support-vector networks, Mach. Learn. 20 (3) (1995) 273–297, https://doi.org/10.1007/bf00994018.
[41] R.J. Schalkoff, Pattern Recognition, Wiley Online Library, 1992.
[42] J. Medina, M. Ojeda-Aciego, Multi-adjoint t-concept lattices, Inf. Sci. 180 (5) (2010) 712–725, https://doi.org/10.1016/j.ins.2009.11.018.
[43] C. Pozna, N. Minculete, R.-E. Precup, L.T. Kóczy, Á. Ballagi, Signatures: definitions, operators and applications to fuzzy modelling, Fuzzy Sets Syst. 201 (2012) 86–104, https://doi.org/10.1016/j.fss.2011.12.016.
[44] C.E. Rasmussen, Gaussian Processes in Machine Learning, Springer, Berlin Heidelberg, 2004, https://doi.org/10.1007/978-3-540-28650-9_4.
[45] M. Sadoughi, C. Hu, C.A. MacKenzie, A.T. Eshghi, S. Lee, Sequential exploration-exploitation with dynamic trade-off for efficient reliability analysis of complex engineered systems, Struct. Multidisc. Optim., doi:https://doi.org/10.1007/s00158-017-1748-7.
[46] M.K. Sadoughi, M. Li, C. Hu, C.A. Mackenzie, High-dimensional reliability analysis of engineered systems involving computationally expensive black-box simulations, in: Volume 2B: 43rd Design Automation Conference, ASME, 2017, https://doi.org/10.1115/detc2017-68273.
[47] M. Sadoughi, A. Downey, C. Hu, S. Laflamme, An iterative signal fusion method for reconstruction of in-plane strain maps from strain measurements by hybrid dense sensor networks, in: 2018 AIAA Information Systems-AIAA Infotech @ Aerospace, American Institute of Aeronautics and Astronautics, 2018, https://doi.org/10.2514/6.2018-0467.
[48] J.P. Lynch, A. Sundararajan, K.H. Law, A.S. Kiremidjian, E. Carryer, Embedding damage detection algorithms in a wireless sensing unit for operational power efficiency, Smart Mater. Struct. 13 (4) (2004) 800–810, https://doi.org/10.1088/0964-1726/13/4/018.
[49] T.-H. Yi, H.-N. Li, Methodology developments in sensor placement for health monitoring of civil infrastructures, Int. J. Distrib. Sensor Netw. 8 (8) (2012) 612726, https://doi.org/10.1155/2012/612726.
[50] E.B. Flynn, M.D. Todd, A bayesian approach to optimal sensor placement for structural health monitoring with application to active sensing, Mech. Syst. Sig. Process. 24 (4) (2010) 891–903, https://doi.org/10.1016/j.ymssp.2009.09.003.
[51] A. Downey, C. Hu, S. Laflamme, Optimal sensor placement within a hybrid dense sensor network using an adaptive genetic algorithm with learning gene pool, Struct. Health Monitor. (2017), https://doi.org/10.1177/1475921717702537, 147592171770253.
[52] S. Laflamme, F. Ubertini, H. Saleem, A. D'Alessandro, A. Downey, H. Ceylan, A.L. Materazzi, Dynamic characterization of a soft elastomeric capacitor for structural health monitoring, J. Struct. Eng. 141 (8) (2015) 04014186, https://doi.org/10.1061/(asce)st.1943-541x.0001151.
[53] H. Saleem, A. Downey, S. Laflamme, M. Kollosche, F. Ubertini, Investigation of dynamic properties of a novel capacitive-based sensing skin for nondestructive testing, Mater. Eval. 73 (10) (2015) 1384–1391. <http://www.scopus.com/inward/record.url?eid=2-s2.0-84948392242&partnerID=MN8TOARS>.
[54] A. Wilkinson, M. Clemens, V. Harding, The effects of SEBS-g-maleic anhydride reaction on the morphology and properties of polypropylene/PA6/SEBS ternary blends, Polymer 45 (15) (2004) 5239–5249, https://doi.org/10.1016/j.polymer.2004.05.033.
[55] S. Laflamme, H.S. Saleem, B.K. Vasan, R.L. Geiger, D. Chen, M.R. Kessler, K. Rajan, Soft elastomeric capacitor network for strain sensing over large surfaces, IEEE/ASME Trans. Mechatron. 18 (6) (2013) 1647–1654, https://doi.org/10.1109/tmech.2013.2283365.
[56] I. Doltsinis, Z. Kang, Robust design of structures using optimization methods, Comp. Meth. Appl. Mech. Eng. 193 (23–26) (2004) 2221–2237, https://doi.org/10.1016/j.cma.2003.12.055.
[57] I. Couckuyt, T. Dhaene, P. Demeester, oodace toolbox: a flexible object-oriented kriging implementation, J. Mach. Learn. Res. 15 (2014) 3183–3186. <http://jmlr.org/papers/v15/couckuyt14a.html>.
[58] Hibbit, Karlsson, Sorensen, ABAQUS/Standard Analysis User's Manual, Hibbit, Karlsson, Sorensen Inc., USA, 2007.